Plunger-type wavemakers with flow: sensitivity analysis and experimental validation

Stephanie Lowell, Johanna McPhee, Rishad A. Irani

Multi-Domain Laboratory, Carleton University, 1125 Colonel By Dr., Ottawa, Ontario, Canada

Abstract

In this paper, the effect of flow on the theoretical model and experimental performance of a plunger-type wavemaker has been investigated. Through a variance-based global sensitivity analysis, the influence of the input parameters on the output variance of the wavemaker model was explored. For a uniform flow, the first order and total effect sensitivity indices were estimated to be $1.29 \pm 0.32\%$ and $6.00 \pm 0.14\%$, respectively. While the flow is less influential compared to the other parameters, it was established that including flow in the model is essential for application to experimental systems. To validate the experimental wavemaker, wave profiles were generated and measured under a variety of test conditions in relation to the sensitivity analysis. It was observed that the error between the experimental results and the theoretical model increased as both frequency and flow increased. To address the observed error, three correction methods were applied to the model which included a case specific, general case, and operational correction. While the case specific correction improved the average a/s percent error by 94.27%, 94.07%, and 96.60% for three different plunger wedges, it was established that the operational correction is more applicable to experimental plunger systems. The operational correction improves the average a/s percent error by 33.14%, 36.63%, and 37.23% respectively for the three wedges. Finally, to further reduce the error between experimental observations and the corrected model, the operational range of the experimental system was established with respect to frequency and flow rate limits.

Keywords: Wave generation, plunger-type wavemaker, water flow, global sensitivity analysis, water channel

1. Introduction

To study advanced hydrodynamics for marine engineering applications such as ship motion and the launch and recovery of tow-bodies, laboratory water channels provide an environment in which applications can be studied under scaled conditions. A schematic (top left) and photograph (bottom left) are provided in Fig. 1 of the Rolling Hills Research Corporation Water Channel [1] at

Carleton University along with the location of a wavemaker. The experimental wavemaker and its various components are also displayed in Fig. 1 in the bottom right. The channel in Fig. 1, whose specifications are given in the top
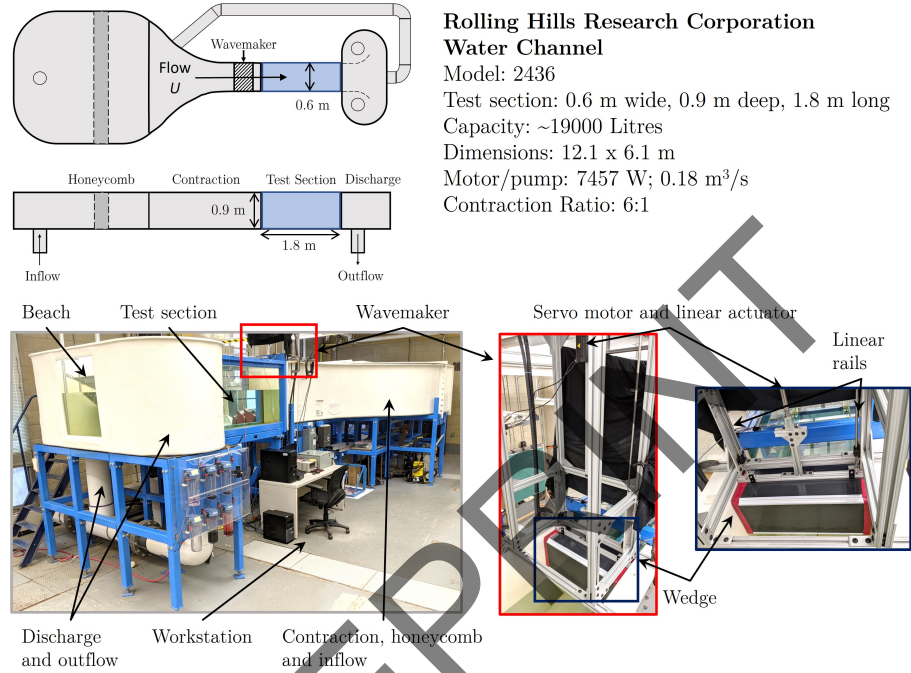

Rolling Hills Research Corporation
Water Channel
Model: 2436
Test section: 0.6 m wide, 0.9 m deep, 1.8 m long
Capacity: ~19000 Litres
Dimensions: 12.1 x 6.1 m
Motor/pump: 7457 W; 0.18 m^3/s
Contraction Ratio: 6:1

Figure 1: Schematic (top left) and photographs (bottom) of the water channel at Carleton University demonstrating the distinct sections of the channel, the direction of flow U, and the location of the wavemaker and its various components. Key specifications for the channel are also included (top right).

right area, is equipped with the ability to produce a uniform flow U through the test section, allowing for direct observations of fluid dynamics through the side of the tank. However, the ability to extend to further applications such as the study of waves and ocean environments is limited, since the original tank was not equipped with a wavemaker. Wavemakers provide an affective method for generating and studying various water waves in a controlled laboratory setting. Therefore, installation of a wavemaker and experimental validation of the system is essential in order to study future hydrodynamics applications in marine engineering. Moveable wall-type wavemakers, such as piston- and flap-types, generate waves through oscillatory motion in the direction of the wave propagation. As such, they require a substantial amount of submerged mechanical components and prohibit the inclusion of flow in the generated wave profile. On the other hand, plunger-type wavemakers, like the one displayed in Fig. 1, form waves by displacing the water through vertical oscillations of a rigid body. Thus, plunger-types are the only wavemaker which allow for flow across the boundary

2

²⁵ and the inclusion of a plunger system would complement the pre-existing equipment for generating flow through the test section. From a preliminary study, Fig. 2 demonstrates as a function of time, the water surface elevation measured by an ultrasonic sensor for waves generated with no flow (top) and with a flow of 0.305 m/s (bottom). In both the no-flow and flow cases, the wavemaker was
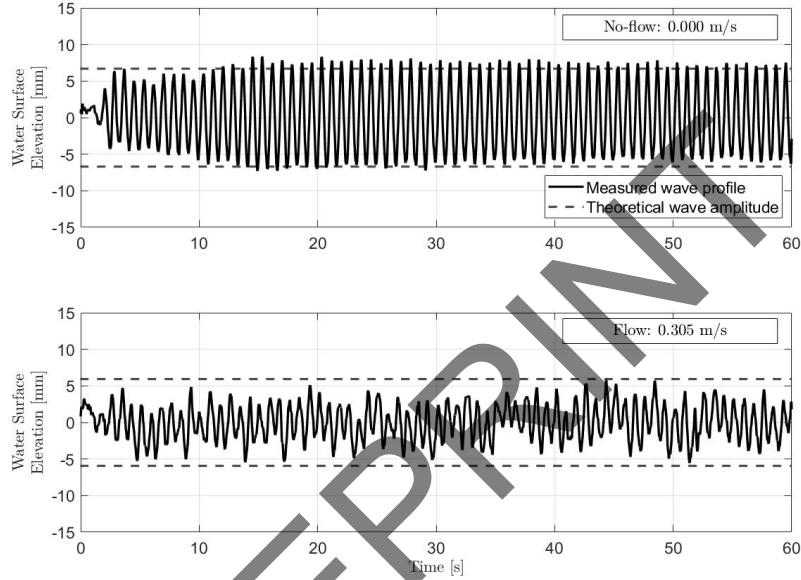

Figure 2: Initial measurement of the wave profile generated by the wavemaker for flow rates of 0.000 m/s (top) and 0.305 m/s (bottom). The waves were produced by a wedge with inner angle $\beta = 25.7°$ and mean depth $d_\mu = 10$ cm. The wavemaker was operated at a frequency $f = 1.2$ Hz and stroke amplitude $s = 0.02$ m, for a water depth of $h = 0.584$ m.

³⁰ oscillated at a frequency of 1.2 Hz, with a stroke amplitude of 2 cm for 60 s. The mean depth of the plunger was also constant between the cases at approximately 10 cm. The no-flow wave profile in Fig. 2 has a maximum recorded peak of 10.22 mm while the maximum for the flow case is 8.32 mm. The time series of the surface elevation for the flow case also appears unsteady, which is ³⁵ attributed to the increase in turbulence at the high flow rate. Comparing the two wave profiles, it is also apparent that the flow impacts the amplitude of the waves; however, prior research and experimental validation of plunger systems has focused on waves generated *without* the influence of flow. The current study aims to address the gap in the literature by including flow in the plunger-type ⁴⁰ wavemaker model for use in applications such as tow body dynamics [2, 3] and launch and recovery [4].

Unlike the more common moveable-wall wavemakers [5], the motion of the plunger allows for flow across the lateral boundary. By using the boundary

3

collocation method, Wu [6] developed a semi-analytical method to study waves
generated by a plunger-type wavemaker that demonstrated the required inclu-
sion of water depth in the wavemaker model. The wave profiles produced by
a plunger-type wavemaker were studied by Ellix and Arumugam [7] which Wu
[6, 8] referenced for comparison to the theoretical model; however, both theory
and experiment were only applied to the still water case and did not include the
effect of flow.

Many researchers have focused on simulations of plunger-type wavemakers to
estimate the generated wave profile in the water channel. As part of a wavemaker
renewal project, Mikkola [9] applied an unstructured finite volume method to
develop a time accurate simulation of a wedge-shaped plunger; however, the
simulation was only conducted for the no-flow case. Similarly, Gadelho et al.
[10] developed a computational fluid dynamics model to study the performance
of a wedge-shaped wavemaker using a Navier-Stokes model to simulate the inter-
action of the wedge with the water. Kashiwagi [11] also presented a numerical
solution for the wavemaker problem; the numerical results of the work along
with those found by Gadelho et al. [10] were compared to a limited number of
experimental results but neither the numerical nor experimental work included
flow. Azadian-Kharanjani et al. [12] investigated the effect of wedge angle
on the wave height, wave amplitude ratio, and wave quality for plunger-type
wavemakers with a constant submerged volume. The numerical work concluded
that the quality of waves decreases with increased wedge angle; however only
waves generated in quiescent water were considered. To further the work in
[12], Nikseresht and Bingham [13] used 2D CFD calculations to study wedge
shape and the influence of the gap between the back of the wedge and the wall
of the tank. A comparison to the linear potential flow theory by Wu [6] was
used to validate the numerical method but both numerical and experimental
results were based on a water channel in which the wedge is in close proximity
to the wall of the tank and the inclusion of flow is not possible. More recently,
He et al. [14] developed a Smoothed Particle Hydrodynamics model in order to
simulate plunger-type wavemakers. The study proved that plunger systems can
be as accurate as the more commonly used piston-type wavemakers; however,
the model did not incorporate flow and was strictly based on the generation of
solitary waves. Hicks et al. [15] investigated non-linear wave generation with a
plunger system wherein a numerical solver was validated against the theoretical
model developed by Wu [6] and a series of experimental tests. The experimental
work included testing twenty different monochromatic waves; however, the work
was conducted under the assumption that no-flow was present. Sun et al. [16]
studied the simulation of linear, Stokes fifth-order, solitary, and irregular waves.
While the simulation did not account for flow, an analysis of wave quality found
that the error in wave amplitude between the developed analytical solutions and
numerical results increased as the inner angle of the wedge increased.

The scope of the current paper investigates the influence of water flow on the
theoretical plunger-type wavemaker model along with an experimental system.
Research into the parameters on which the wavemaker model is dependent will
be determined through a variance-based global sensitivity analysis (GSA) [17].

4

₉₀ As a result of the analysis, the impact and understanding of flow on the design and operation of a plunger-type wavemaker is an essential contribution to the field. The present study also seeks to provide insight to the input parameters for the wavemaker model through an experimental analysis of the system for a wide variety of testing conditions. In doing so, improvements to the theoretical ₉₅ model through correction factors can be identified and applied. Thus, the study will yield further understanding towards the strengths and weaknesses of the wavemaker model and a basis for the design of plunger-type systems.

In Section 2, the theory governing the wavemaker model for the inclusion of flow is described. Building on the authors' previous work [18], Section 3 presents ₁₀₀ the global sensitivity analysis theory along with the results of the analysis for the plunger-type wavemaker model. The design of the experimental wavemaker and accompanying experimental considerations are described in Section 4 followed by the results of the experimental testing in Section 5. Finally, conclusions are summarized in Section 6.

₁₀₅ 2. Plunger-type Wavemaker Theory

The plunger-type wavemaker problem for a wedge with a triangular cross-section in a laboratory water channel is represented by the diagram displayed in Fig. 3. Here, x represents the horizontal axis and z is the vertical axis, while
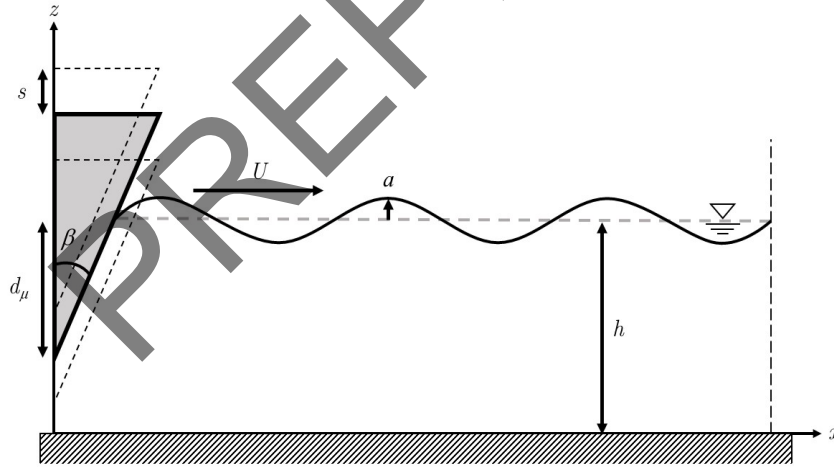

Figure 3: Schematic of a plunger-type wavemaker in a laboratory water channel with flow U.

the width of the channel is assumed to be represented by a semi-infinite bound-₁₁₀ ary. The inner angle of the wedge β is measured between the vertical z axis and the hypotenuse of the wedge, while the mean wedge depth d_μ is measured

with reference to the still water depth h. Since d_μ represents an average distance measured during wave generation, the parameter is independent of time. Relative to the plane $z = h$, the amplitude a measures the maximum distance
115 between the plane and the crest of the produced wave. Forward, propagating waves are generated by the vertical displacement s of the plunger as it oscillates in the water column. Thus, the water wave length and amplitude are controlled by the oscillation frequency and fluid displacement of the plunger. The oscillating motion allows for flow across the lateral boundary throughout the duration
120 of the operation. The magnitude of the mean water flow U is positive along the x-axis when moving the same direction as the waves produced by the wavemaker. One should note that in previous work [9, 10, 11, 14, 15] the water flow U was zero, whereas in the current work, $U \geq 0$.

The relationship between the wave amplitude a and the stroke amplitude of
125 the plunger s provides an important metric for wavemaker design. For a known stroke amplitude, the wave amplitude a is determined from the wave profile produced by the wavemaker. Under the assumption of classic hydrodynamics, the fluid flow is inviscid, incompressible, and irrotational [19]. The theoretical model for a triangular plunger-type wavemaker which includes flow and relates
130 the water wave amplitude a to the stroke amplitude s is given by,

$$\frac{a}{s} = \left| -i_m A_1' k_p h \sinh(k_p h) \right|, \tag{1}$$

where i_m is the imaginary number, k_p is the progressive wavenumber, and h is the still water depth [18, 20]. A_1' is a coefficient whose value is determined using Wu's [6] boundary collocation method based on a velocity potential consisting of one progressive wave and a number of standing waves which dissipate expo-
135 nentially. A detailed derivation of the a/s model (1) is available for reference in Appendix A.

A uniform flow U has been included in the model through modification of the dispersion relation which governs the wave profile. For the no-flow condition, the velocity potential of the water's free surface is constrained by the dispersion
140 relation given by,

$$\omega^2 = gk_p \tanh(k_p h), \tag{2}$$

where g is gravitational acceleration [6]; however, in the presence of a uniform flow U, water waves will experience a Doppler shift. To account for a flow rate U, the frequency ω within the dispersion relation for the plunger-type wavemaker problem is shifted such that [19],

$$(\omega - k_p U)^2 = gk_p \tanh(k_p h). \tag{3}$$

145 From the definition of phase velocity where the celerity C is equal to ω/k_p, (3) can be rewritten as [19],

$$(C - U)^2 = \frac{g}{k_p} \tanh(k_p h). \tag{4}$$

For deep water, the solution to the dispersion relation in (4) with regards to C is determined using a quadratic solution and replacing the wavenumber k_p with ω/C [19], such that,

$$C = \left(U + \frac{g}{2\omega}\right) + \sqrt{\frac{Ug}{\omega} + \frac{1}{4}\left(\frac{g}{\omega}\right)^2}. \tag{5}$$

150 The definition of the celerity C in (5) provides the wave speed for a progressive wave in the presence of a uniform flow $U \geq 0$. Thus, the progressive wavenumber can be determined analytically by,

$$k_p = \frac{\omega}{C} = \frac{\omega}{\left(U + \frac{g}{2\omega}\right) + \sqrt{\frac{Ug}{\omega} + \frac{1}{4}\left(\frac{g}{\omega}\right)^2}}, \tag{6}$$

such that a flow $U \geq 0$ is taken into consideration for the plunger-type wavemaker model in equation (1) [19]. Moving forward, the theoretical model used
155 herein which includes flow will be referred to as the plunger-type flow (PTF) model, while the standard model established by Wu [6] which does not include flow will be referred to as the Wu model. Note that the Wu model, and by extension the PTF model, were derived specifically for plunger's with a triangular cross section. Other shapes, such as cylinders, could prove useful in increasing
160 fluid displacement while decreasing hindrance to the surface flow, but would require modification to the current model. Therefore, a general form model which accounts for any shaped plunger with flow is an avenue for potential future work.

The PTF model has six input parameters: flow U, wave frequency ω, wedge angle β, mean wedge depth d_μ, water depth h, and the number of node points
165 M in the boundary problem. The water flow U, along with the wave frequency ω, will impact the value of the progressive wavenumber k_p. The progressive wavenumber is also required to determine A'_1; hence, A'_1 will be dependent on U and ω, in addition to h, d_μ, β, and M. While the number of boundary node points M is not a physical parameter, Wu [6] showed that the choice in M did
170 have an effect on the amplitude ratio a/s. Therefore, to verify the influence of M on the model, the number of boundary node points has been included as an input parameter in the current study. Although the PTF model in (1) has the same form of the Wu model, the output of the PTF model is affected by the inclusion of flow. Fig. 4 compares the effect of applying a uniform flow U on the
175 amplitude ratio a/s for the PTF model (squares) and the Wu model (circles). For the models in Fig. 4, the remaining input parameters have been fixed to the conditions observed in Fig. 2 where $f = 1.2$ Hz, $\beta = 25.7°$, $d_\mu = 10$ cm, $h = 0.583$ m, and $M = 200$. Since the Wu model is independent of U, the value of a/s remains constant and equal to the value of a/s for $U = 0$. Conversely,
180 the PTF model indicates that for a constant stroke amplitude s, the generated wave amplitude a will decrease with the inclusion of flow; an observation which is available when comparing the top and bottom plots of Fig. 2. While the general relationship between a/s and U for the PTF model in Fig. 4 is consistent, the exact value of a/s will also be dependent on the values of the input parameters
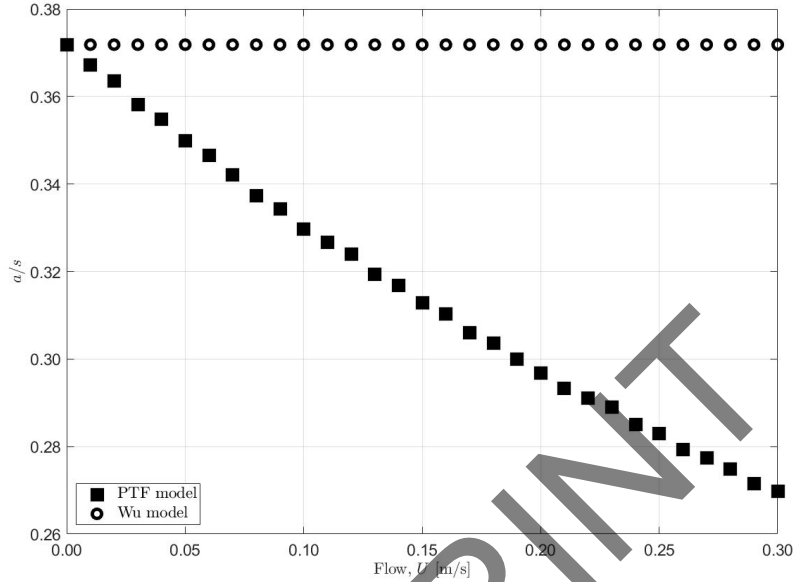
7

Figure 4: The ratio of the wave amplitude to stroke amplitude for a uniform flow as predicted by the plunger-type flow (PTF) model which incorporates U and the standard Wu model which does not include U. The values of the remaining input parameters were fixed at $f = 1.2$ Hz, $\beta = 25.7°$, $d_\mu = 10$ cm, $h = 0.58$ m, and $M = 200$.

which include the flow U, wave frequency ω, wedge angle β, mean wedge depth d_μ, water depth h, and node points M. The relative influence of the six input parameters on the output of the PTF wavemaker model was quantified through a variance-based global sensitivity analysis.

3. Global Sensitivity Analysis

Various methods exist for conducting a sensitivity analysis, the use of each method being dependent on the computational expense and the complexity of the model, among other constraints. For a full exploration of the input space for the PTF model, a variance-based global sensitivity analysis (VBGSA) was chosen. Assuming the input parameters are not deterministic and are independent of one another, VBGSA makes use of sensitivity indices S as a measure of the influence a parameter has on a model including both first- and higher-order effects. Therefore, the goal of the sensitivity analysis in this paper was to determine the sensitivity indices for each input parameter of the wavemaker model. Currently, VBGSA is used across many fields with the main focus on design optimization applications [21, 22, 23, 24, 25]. Specifically, in the marine engineering field, sensitivity analysis has been instrumental for applications such as ship design [26, 27] and modelling ship motion [28, 29].

8

In VBGSA, for a model represented by the form $Y = f(X_1, X_2, \ldots, X_k)$ where Y is a scalar output and X_i is the model's input parameters for $i = 1, 2, \ldots, k$, there exists $2^k - 1$ sensitivity indices. The sensitivity indices estimated herein were numerically computed using the Monte Carlo sampling methods presented by Saltelli et al. [30]. The first order sensitivity index S_i estimates the independent contribution of each parameter i to the output variance of the wavemaker model. As such, S_i is the ratio of the partial variance V_i taken over X_i to the overall variance of the model V and is numerically estimated by the expression,

$$S_i = \frac{V_i}{V} = \frac{\frac{1}{N_s}\sum_{j=1}^{N_s} f(\mathbf{H})_j \left(f(\mathbf{G_H}^{(i)})_j - f(\mathbf{G})_j \right)}{\frac{1}{N_s}\sum_{j=1}^{N_s} \left(f(\mathbf{G})_j \right)^2 - \frac{1}{N_s}\sum_{j=1}^{N_s} f(\mathbf{G})_j f(\mathbf{H})_j}, \tag{7}$$

where N_s represents the number of samples used in the Monte Carlo analysis and is consistent for all parameters [30]. $f(\cdot)_j$ is the model evaluation of the jth row of matrices G, H, and G_H constructed for the analysis, the forms of which matrices are provided in Appendix B. For higher order effects, total effect sensitivity indices S_{Ti} were considered in order to reduce the computational expense of the VBGSA [31]. S_{Ti} includes the first order effect of a parameter i, along with all higher order effects involving the specified parameter and is estimated using the expression [30, 32],

$$S_{Ti} = \frac{V_{Ti}}{V} = \frac{\frac{1}{2N_s}\sum_{j=1}^{N_s} \left(f(\mathbf{G})_j - f(\mathbf{G_H}^{(i)})_j \right)^2}{\frac{1}{N_s}\sum_{j=1}^{N_s} \left(f(\mathbf{G})_j \right)^2 - \frac{1}{N_s}\sum_{j=1}^{N_s} f(\mathbf{G})_j f(\mathbf{H})_j}. \tag{8}$$

By using the approach of S_{Ti}, only $2k$ indices need to be determined and the values of the indices can be used to differentiate between influential and non-influential parameters in the PTF model. For instance, uncertainty in a parameter whose total effect index is zero will not significantly impact the output of the model and can be set to a deterministic value.

The uncertainty for the estimation of each sensitivity index was determined by calculating its respective 95% confidence interval. Using error propagation on S_i and S_{Ti} in (7) and (8) respectively, the uncertainty associated with the first order δS_i and total effect δS_{Ti} sensitivity indices take the following forms,

$$\delta S_i = \left[\left(\frac{\delta V_i}{V} \right)^2 + \left(\frac{V_i \delta V}{V^2} \right)^2 \right]^{1/2}, \tag{9}$$

$$\delta S_{Ti} = \left[\left(\frac{\delta V_{Ti}}{V} \right)^2 + \left(\frac{V_{Ti} \delta V}{V^2} \right)^2 \right]^{1/2}. \tag{10}$$

Here, δV_i, δV_{Ti}, and δV represent the uncertainty in the first order, total effect, and model variance, respectively. A numerical method for the uncertainty in variance from Griffiths [33] was applied to each term, the final forms of which are provided in Appendix B. Using the numerical estimators presented, the first order and total effect sensitivity indices for the PTF model were determined.

3.1. GSA Results

²³⁵ For each of the input parameters, the VBGSA required a sample distribution of values for use in the Monte Carlo analysis. The uniform distribution for the six input parameters U, ω, β, d_μ, h, and M are outlined in Table 1 along with the results of the sensitivity analysis. The parameter distribution ranges represent

Table 1: Uniform parameter distribution along with the percent sensitivity indices and error for the PTF wavemaker model.

Param.	Min.	Max.	$\mathbf{S_i}$ [%]	$\delta\mathbf{S_i}$ [%]	$\mathbf{S_{Ti}}$ [%]	$\delta\mathbf{S_{Ti}}$ [%]
U	0.0 [m/s]	2.5 [m/s]	1.29	$\pm$ 0.32	6.00	$\pm$ 0.14
ω	0.4π [rad/s]	10π [rad/s]	19.41	$\pm$ 0.83	42.16	$\pm$ 0.97
β	20 [Deg]	75 [Deg]	7.49	$\pm$ 0.69	27.36	$\pm$ 0.61
d_μ	0.05 [m]	0.40 [m]	7.54	$\pm$ 0.51	15.06	$\pm$ 0.35
h	0.50 [m]	2.5 [m]	2.01	$\pm$ 0.24	2.82	$\pm$ 0.09
M	50	400	0.03	$\pm$ 0.04	0.09	$\pm$ 0.00

values typically observed in laboratory environments, taking into consideration ²⁴⁰ various configurations of both the wedge and water channel and a wide range of frequencies and flow rates. The specific range for the number of boundary nodes points M was chosen in reference to the range suggested by Wu [6]. Using the ranges in Table 1, the first order and total effect sensitivity indices were determined for each parameter in the PTF model, along with the uncertainty ²⁴⁵ associated with each estimate.

The frequency ω was determined by the sensitivity analysis to have the highest impact on the output variance of the wavemaker model. From a design standpoint, uncertainty in the model will therefore be governed by uncertainty in the wave frequency. To lower the uncertainty in a/s for experimental testing, ²⁵⁰ reducing the uncertainty measurement in the frequency should be prioritized. Comparatively, the number of boundary node points M has the lowest sensitivity indices which are notably close to zero. Consequently, it can be concluded that the number of node points does not individually impact the output variance of the PTF model; therefore, M can be deemed a non-influential parameter and ²⁵⁵ set to a fixed value. In regards to the wedge angle β and mean wedge depth d_μ, the dimensions and positioning of the wedge should also be measured with reduced uncertainty as those parameters have the second and third highest influences on the output of the model.

The VBGSA also revealed low sensitivity indices for the water depth h. In ²⁶⁰ the assessment of the Wu model, Wu [6] concluded that even under the assumption of deep-water conditions, water depth was a very important parameter in the wavemaker model; however, it was determined herein that for a general sample distribution of the input parameters, h had the lowest impact compared to the remaining influential parameters. Although the depth of the water must still

10

₂₆₅ be included in the model for hydrodynamic considerations, the lower indices indicate that uncertainty in the measurement will not generate large uncertainties in the model.

From Table 1, the sensitivity indices for the flow U were estimated to be $S_U = 1.29 \pm 0.32\%$ and $S_{TU} = 6.00 \pm 0.14\%$. Despite the relatively low influence of
₂₇₀ U compared to the other parameters, variation in the flow causes an observable change in a/s as shown in Fig. 2. Since S_{TU} includes the higher order effects due to the interaction of U with the other five parameters and S_U, $S_{TU} - S_U = 4.71 \pm 0.35\%$ indicates that the effect is mostly attributable to the higher order indices and the inclusion of the flow in the PTF model is essential. As such,
₂₇₅ physical systems must also take flow rate into consideration, the impact of which was determined through experimental validation.

4. Experimental Design

4.1. Wavemaker Considerations

The plunger-type wavemaker shown in Fig. 1 operates by vertically oscil-
₂₈₀ lating a triangular-shaped wedge in the water in order to generate waves. The desired wave pattern is thus dependent on the design of the wavemaker along with the parameters which govern its movement. The wavemaker used herein is supported by a vertical structure built with extruded t-slotted aluminium members. A linear actuator is fixed to the structure with its actuating rod pointing
₂₈₅ vertically down towards the water's surface. The triangular-shaped wedge, the details of which are displayed in the bottom right of Fig. 1, is attached to the end of the rod through a carriage system which is equipped with linear guide rails to maintain the position of the wedge relative to the sides of the water channel as it oscillates. The wedge is the only component of the wavemaker which
₂₉₀ makes contact with the water and can be efficiently interchanged with wedges of other sizes. The motion of the wavemaker is governed by the displacement of an actuating rod. The sensitivity analysis revealed that the wavemaker model is most sensitive to uncertainty in the wavemaker frequency. To decrease the uncertainty, a high-precision linear actuator was used, manufactured by Thomson
₂₉₅ [34], which was determined to have an average of 0.04% error between the set frequency and the true frequency of the system. The linear actuator, is accompanied by a Kollmorgen servo motor [35] and drive [36] which was controlled through a National Instruments DAQ system. Using LabVIEW, the setpoint of the actuator and its specific motion for a desired wave profile are controlled. The
₃₀₀ wave profile is measured simultaneously during wave generation using a SICK ultrasonic sensor [37] with an accuracy of $\pm 1\%$, located in the test section of the water channel, and pointing directly towards the water surface.

There are pre-existing factors that must be taken into consideration for the initial design and operating range of the wavemaker. The actuator has a max-
₃₀₅ imum acceleration of 6 [m/s^2] which must be taken into consideration with respect to the frequency and the stroke amplitude of the sinusoidal wave. The

11

frequency f of the wavemaker is related to the stroke amplitude s of the actuator through the expression,

$$f = \frac{1}{2\pi}\sqrt{\frac{a_a}{s}}, \tag{11}$$

where a_a is the acceleration of the actuator. Substituting the maximum acceleration of the actuator into (11) provides an upper limit on the frequencies and corresponding stroke amplitudes that can be achieved with the wavemaker. The height of the wedge also limits the available stroke amplitude of the wavemaker. For the experimental system used herein, the operational limit for the stroke amplitude was 0.06 m. The intersection of the actuator and the operational wedge limit creates an initial range in which to operate the wavemaker with respect to both frequency and stroke amplitude. Further limitations may exist depending on the performance of the wavemaker which were explored through experimental testing.

Experimental work with plunger-type wavemakers in literature is often limited to testing a single frequency or stroke amplitude and without the inclusion of flow [9, 10]. To develop a full understanding of the operational limits of the plunger system, each of the influential parameters in the sensitivity analysis were investigated in experimental testing of the wavemaker including the flow rate U, frequency ω, wedge angle θ, and wedge mean depth d_μ. The design of the wavemaker was explored by measuring the amplitude of regular waves generated by three different wedge-shaped plungers to address the wedge angle parameter. Wedge A has an inner angle $\beta = 25.7°$, Wedge B has $\beta = 35.0°$, and Wedge C has $\beta = 45.0°$. Along with the wedge angle, the sensitivity analysis of the wavemaker model showed that the frequency, mean wedge depth, and flow parameters interacted the most with one another. To ensure that the wedge angle remains constant during testing, the wedges are constructed from 1/4" solid PVC and fitted with inner supports. The uncertainty in the frequency and mean wedge depth is decreased through the use of the high-precision linear actuator to which the wedges are attached. While the flow rate can not be measured as accurately, its uncertainty is not as influential compared to the previously mentioned parameters. On the other hand, although the sensitivity analysis showed that the water depth interacts with the other parameters in the wavemaker model as well, it was not tested as an experimental parameter since it was difficult to vary the water depth in the water channel. Therefore, the impact of frequency, mean wedge depth, and flow were tested for each wedge angle. In addition, to evaluate an experimental a/s, various stroke amplitudes were also tested. Fig. 5 displays the range of tests performed as a function of frequency and stroke amplitude in relation to the operational range of the wavemaker. For each wedge, the 20 tests shown in Fig. 5 were repeated at mean wedge depths of 10 cm, 12 cm, and 14 cm which in turn were repeated at five significant flow rates of 0.000 m/s (0.00 in/s), 0.076 m/s (3.00 in/s), 0.152 m/s (6.00 in/s), 0.229 m/s (9.00 in/s), and 0.305 m/s (12.00 in/s). In total, 900 experimental tests were performed with the plunger-type wavemaker. The test points in Fig.
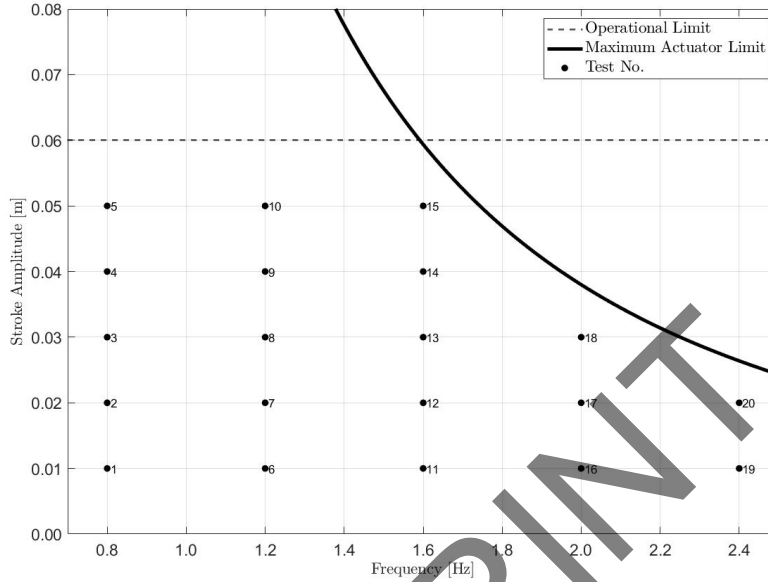
Figure 5: The range in experimental tests with regards to frequency and stroke amplitude along with the limits of the wedge and actuator.

5 were chosen to cover the majority of the initial operating range of the wave-
350 maker. The mean depths were chosen such that hypothetically, a large enough wave would still be generated for the range in tested stroke amplitudes. The range in the flow values was chosen based on the maximum available flow rate for the water channel. As such, the impact of the flow, frequency, wedge angle, wedge mean depth, and stroke amplitude were investigated experimentally to
355 evaluate the performance of the wavemaker and the system's limitations.

4.2. Water Channel Considerations

Along with the wavemaker and measurement sensors, the water channel is also equipped with a wave absorber to reduce the amount of wave reflection. The reflection coefficient, define as the ratio of the reflected wave height to
360 the incident wave height, was determined following the methodology presented by Suh et al. [38] for wave reflections in the presence of flow. For the tests performed in this study, the average reflection coefficient was determined to be 0.36, such that the wave reflection in the water channel is not a dominant effect.

The still water depth was nominally set at 0.60 m, but did vary from 0.58 to
365 0.63 m throughout the duration of the experimental tests which took place over multiple days. The water depth was therefore measured each day of testing and the small fluctuations were included in the post-process analysis. Additionally, in the derivation of the PTF model, deep-water conditions were assumed with

respect to the celerity C in (5). The deep-water condition requires,

$$h > 0.5L, \tag{12}$$

370 where h is the water depth and L is the wavelength. When the deep-water condition is satisfied, the celerity of the waves are dependent on flow U, frequency ω, and gravitational acceleration g. On the other hand, if the condition is not met, the waves are in shallow water and the celerity is governed by the water depth h, flow U, and gravitational acceleration g, such that,

$$C = U + \sqrt{gh}. \tag{13}$$

375 For the results presented in the following section, the theoretical value for the PTF model were derived assuming the deep-water condition to be true. Therefore, in a post-process analysis, satisfaction of the condition was investigated for the 900 experimental tests outlined in Section 4.1. To determine the wavelength of the generated waves, the wave profile was measured by two ultrasonic 380 sensors, separated along the x-axis of the water channel by a distance of $\Delta x = 0.31$ m. Using the two wave profiles, the difference in time Δt between wave crests measured by the first and second sensor were determined and averaged over a 10 s interval within the total time series corresponding to steady state. Thus, the approximate wavelength of the generated waves was determined by,

$$L = \frac{\Delta x}{f \Delta t}, \tag{14}$$

385 where f is the measured experimental frequency and $\Delta x/\Delta t$ corresponds to the celerity of the wave. Comparing the determined wavelength to the appropriate water height in each test, it was found that the deep water condition was satisfied for 605 out of the 900 experimental tests. For the remaining tests, wherein the deep water condition was not satisfied, the corresponding frequencies were $f \leq$ 390 1.2 Hz. Therefore, assumption of the deep water condition in the PTF model is justified for the majority of the tests.

The overall flow rate in the channel is regulated using a digital readout in increments of 0.1 in/s. For the current setup, only wave-following-flow conditions were implemented since the direction of the flow cannot be changed. 395 By changing the placement of the wavemaker to face in the opposite direction, wave-against-flow conditions could be explored in future work. Unlike piston- and flap-type wavemakers, plunger-type wavemakers allow flow to move across the lateral boundary; however, the wavemaker will still hinder the flow around the submerged volume leading to turbulent flow fields in front of the wave- 400 maker. Since the flow is assumed to be uniform in the PTF model, it is critical to identify the effect of the wavemaker on the flow. Figure 6 demonstrates the movement of the flow in the test section of the channel for the scenario in which the wavemaker is generating waves, and for the scenario where there is no wave-maker in the water. The dispersion of blue dye was used to visualize the flow 405 at four different depths in the tank corresponding to $H_1 = 0.55$ m, $H_2 = 0.45$

14

With Wavemaker   Without Wavemaker
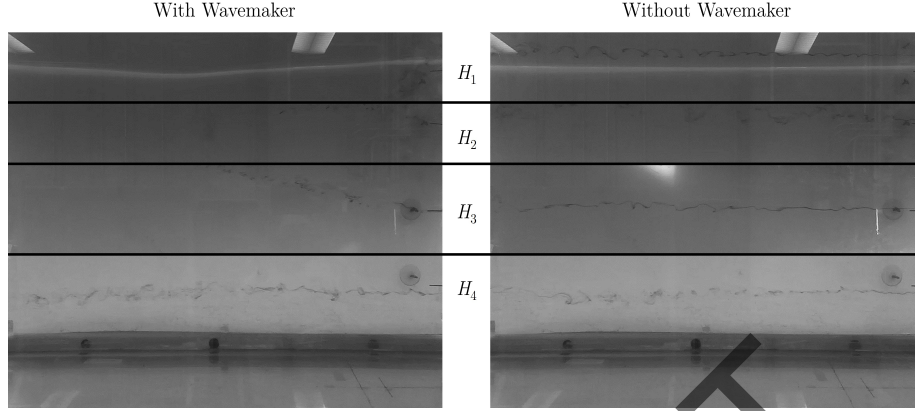
H_1

H_2

H_3

H_4

Figure 6: Turbulence in the water channel test section when the wavemaker is submerged and moving (left) and when no wavemaker is present (right). Relative to the bottom of the tank, the dye system was implemented at four depths in the water, $H_1 = 0.55$ m, $H_2 = 0.45$ m, $H_3 = 0.30$ m, and $H_4 = 0.16$ m, with the total water depth $h = 0.60$ m.

m, $H_3 = 0.30$ m, and $H_4 = 0.16$ m, with the total water depth $h = 0.60$ m as measured from the bottom boundary of the channel. The flow was set to 0.076 m/s, and for the scenario in which the wavemaker is included, $f =1.2$ Hz, $d_\mu =$ 0.12 m, $\beta=35.0°$, and $s = 0.03$ m. The lack of clear flow line near the surface when the wavemaker is active is due to turbulence and mixing; however, near the bottom of the tank, visually, the flows are comparable with and without the wavemaker in the water. As such, the turbulence caused by the presence of the wavemaker may be a source of error between the wave amplitudes measured experimental and those predicted by the PTF model in which uniform flow is assumed. Due to the non-trivial nature of the situation, the exact velocity profile has not been determined for this study. While the flow is influenced by the wavemaker, the authors make no assumption on the quantitative motion of the flow in the test section and instead, the current work focuses strictly on the generated wave profiles. With these considerations on both the wavemaker and the water channel, the performance of the wavemaker system was evaluated for generating regular waves.

5. Experimental Results and Correction Methods

The output of the proposed PTF model is the wave amplitude to wavemaker stroke amplitude ratio a/s. Hence, a/s is the key metric for evaluating the performance and operational range of the experimental wavemaker. To compare the values of a/s as measured experimentally and predicted by the proposed model, the following analysis will consider the percent error expressed by,

$$\% \text{ Error} = \left| \frac{\text{Proposed} - \text{Experimental}}{\text{Experimental}} \right| \times 100\%, \tag{15}$$

15

where "experimental" refers to the measured a/s and "proposed" corresponds to the value as predicted by the PTF model. For the form of the error metric to
430 apply, it is assumed that the experimental values measured with the ultrasonic sensor represent truth data, with the aim to bring the model closer to experimental results. In doing so, the validity of the proposed model as it applies to real wave-flow interactions can be examined. The set of 900 tests outlined in previous section were then analyzed and a/s for each test was determined for
435 comparison to the proposed model. Note that in determining the theoretical a/s, the experimental values of each input parameter were used as an input to the semi-analytical solution. An example wave profile generated by wedge A (β = 25.7°) is displayed in Fig. 7 along with the theoretical wave for the no-flow (top) and 0.076 m/s flow case (bottom). For both cases, the wavemaker has a
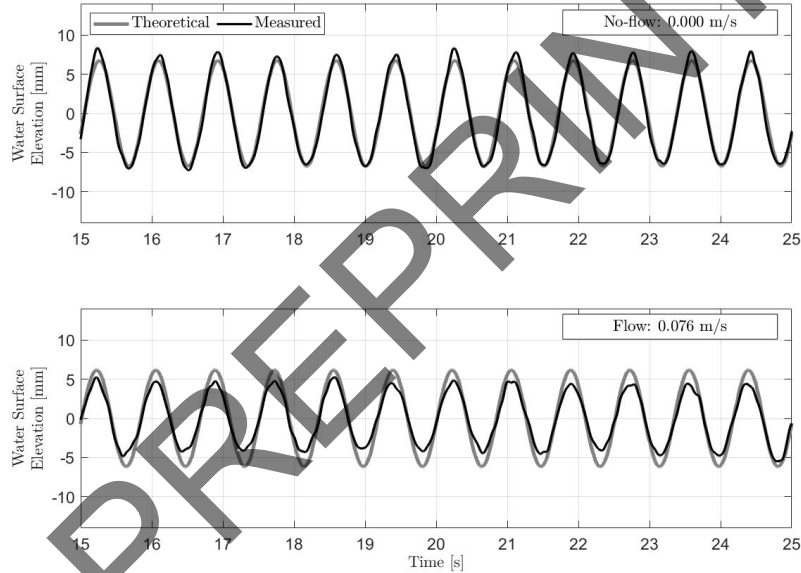

Figure 7: The measured and theoretical wave profile for generated waves with and without flow.

440 frequency of 1.2 Hz, a set stroke amplitude of 2 cm, and a mean depth of 10 cm. For the no-flow case in Fig. 7, the theoretical amplitude of the generated waves was 6.74 mm while the average measured amplitude was 7.26±0.23 mm. For the flow case, the theoretical amplitude was 6.15 mm while the average measured amplitude 4.59±0.23 mm. As a result, in the no-flow case, the model
445 underestimated the generated wave amplitude while in the flow case, the theoretical amplitude is overestimated. Nevertheless, the impact of flow can be observed in both the theoretical and experimental wave profiles. Note that the flow case in Fig. 7 appears more steady in time than compared to the flow

16

case in Fig. 2, since the turbulence in the channel increases with increased flow
rate. Therefore, it is important that the inclusion of flow be investigated for the
experimental plunger-type wavemaker.

To determine the operational range and assess the performance of the wave-
maker, observing the results of all 900 tests was critical. To do so, the percent
error is plotted as function of the dimensionless parameter kb, where k is the
wavenumber and b is the mean width of the plunger wedge. The wavenumber
k is given as,

$$k = \frac{\omega}{\left(U + \frac{g}{2\omega}\right) + \sqrt{\frac{Ug}{\omega} + \frac{1}{4}\left(\frac{g}{\omega}\right)^2}}, \tag{16}$$

where $\omega = 2\pi f$ is the wave frequency, U is the flow rate, and g is the gravita-
tional acceleration [19]. The mean width of the plunger b can be determined
based on the geometry of the triangular cross-section of the wedge by,

$$b = d_\mu \tan\beta, \tag{17}$$

where d_μ is the mean depth of the plunger wedge and β is the inner angle of
the wedge with respect to the vertical. As such, the dimensionless parameter
kb accounts for each of the sensitivity analysis parameters: the frequency f,
flow rate U, mean wedge depth d_μ, and wedge angle β. Fig. 8 displays the a/s
percent error for wedge A as a function of kb, separated by the five tested flow
rates. Each point represents a single experimental test including each mean
depth as well as the multiple stroke amplitudes. Averaging over all tests for
each wedge, the average percent error between the model and the experimental
results is 58.13% for wedge A. The maximum % error occurs at a flow rate of
0.305 m/s for $kb = 0.86$ and is 492.72% while the minimum % error at $kb =$
0.14 is 0.01% for a flow rate of 0.076 m/s. Similar results for wedges B and C
are displayed in Fig. 9 and Fig. 10, respectively. The overall percent error
between the model and experiment for wedge B was 48.04% with the maximum
error occurring for a flow rate of 0.305 m/s at kb=0.89 and equal to 336.15%.
The minimum % error for wedge B is observed in the no flow case (0.000 m/s) at
kb=0.22 and equal to 0.09%. Similarly, the percent error observed throughout
the tests performed with wedge C had an average of 72.78%. The maximum
error of 493.03% is at kb=1.53 for U=0.305 m/s while the minimum error of
0.21% is at kb=3.25 for U=0.000 m/s. Overall, the value of a/s in 795/900
experimental tests were overestimated by the PTF model with the remaining
105 underestimated cases occurring more frequently in the no-flow tests at the
lowest values of kb.

In general, wedge B generates waves with amplitude closest to the predicted
model; however, there is still a large deviation from theory and the percent error
tends to increase with increasing kb value, especially at the higher flow rates.
For a single flow rate, kb is mostly dependent on the frequency ω; thus, the
observed increase in error between theory and experiment could be attributed
to the increase in frequency. The increase in percent error due to the flow rate
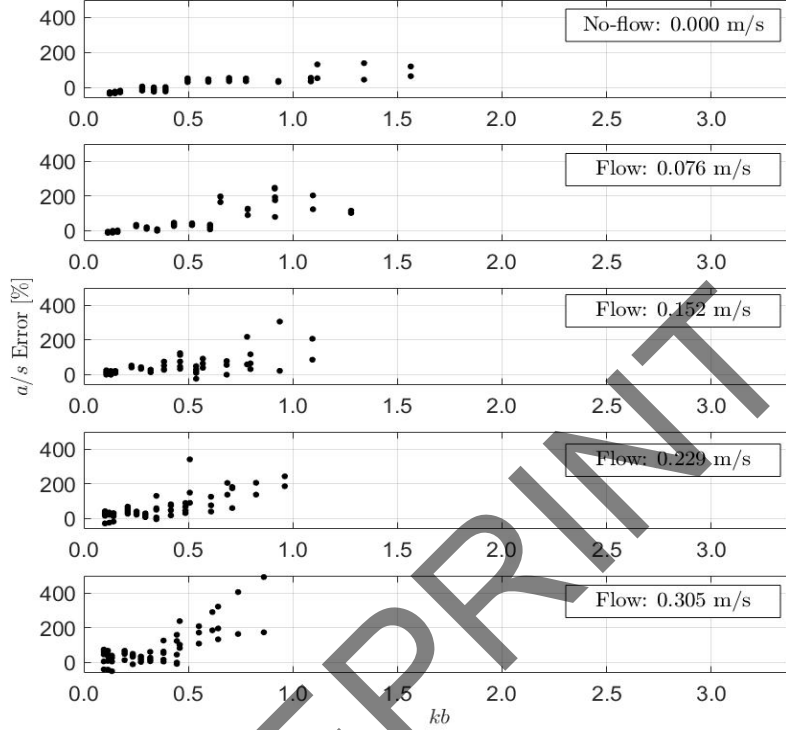
17

Figure 8: a/s percent error for wedge A as a function of kb for the five tested flow rates.

further suggests that using lower flow rates will result in waves that can be more closely predicted by the model. Further error may be due to external ⁴⁹⁰ factors within the water channel and complex hydrodynamics phenomena that are not taken into account in the theoretical model such as leakage around the wedge, reflection of the waves off the walls of the water channel, and turbulence caused by the wavemaker's hindrance to the surface flow. Additionally, Wu's [6] original model assumed only down stream waves; however, in the current setup, ⁴⁹⁵ the wavemaker is at the entrance of the test section. Therefore, disturbances could propagate upstream which is not explicitly accounted for in the proposed model. To account for various sources of error and unmodeled phenomena in the proposed PTF model, we propose three corrections methods.

5.1. Model Correction

⁵⁰⁰ To accommodate for the discrepancies observed in the amplitude to stroke ratio between the experimental and theoretical values, three different methods were explored to apply a correction to the PTF model. In doing so, it is de-
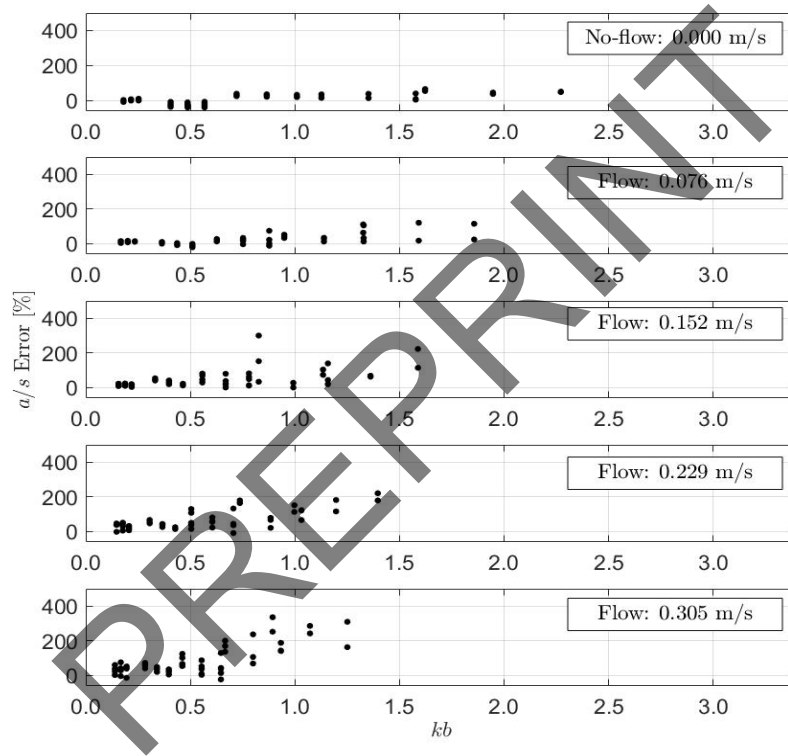
18

Figure 9: a/s percent error for wedge B as a function of kb for the five tested flow rates.
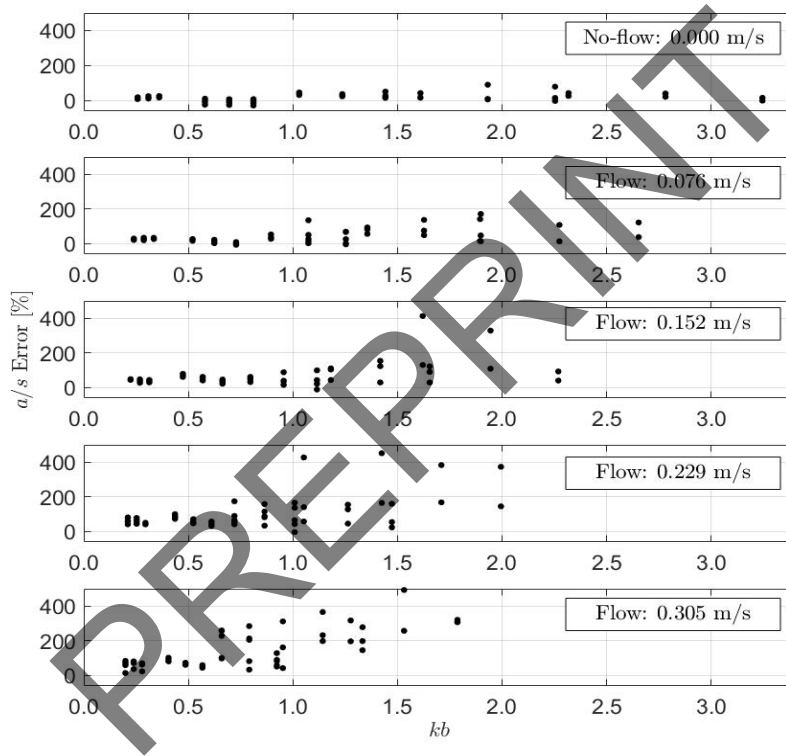
Figure 10: a/s percent error for wedge C as a function of kb for the five tested flow rates.

sired that the model will better represent the experimental results that were observed. The methods include a case specific correction, a general correction, and an operational correction. The correction factors empirically account for turbulence or other complex hydrodynamic effects as explicitly modelling these phenomena is outside the scope of the current study. Since the majority of the experimental tests indicated that the model was over-predicting the amplitude of the generated waves, all three methods work to decrease the value of a/s in the model.

5.1.1. Case Specific Correction

The first method for correcting the model will be referred to as the case specific correction and is based on the standard deviation of a given wave profile. For the experimental results to match that of the model, they should both have the same standard deviation. For cases where the standard deviations are not the same, the model can be scaled to match the distribution of the experimental case by a correction factor ζ given by,

$$\zeta = \frac{\sigma_e}{\sigma_m},\tag{18}$$

where σ_e is the standard deviation of the experimental wave profile and σ_m is the standard deviation of the theoretical wave profile. The correction factor is determined based on the normalized output z_e of the experimental wave profile. Normalizing the experimental data to have a zero mean and a standard deviation of one can be achieved using the expression,

$$z_e = \frac{x_i - x}{\sigma_e},\tag{19}$$

where x_i is a data point and x is the average of all points. The theoretical wave profile z_{me} normalized with respect to the experimental can be achieved using the expression,

$$z_{me} = \frac{x_i - x}{\sigma_e},\tag{20}$$

where the closer that z_{me} is to a value of one, the closer the theoretical wave profile matches that of the experimental. To force the model to match the experimental, the normalized model requires a standard deviation of one, denoted as z_m and given by,

$$z_m = \frac{x_i - x}{\sigma_m}.\tag{21}$$

Scaling the theoretical data to match that of the experimental, denoted by $x_{i-scaled}$ can be accomplished by,

$$x_{i-scaled} = (x_i - x)\zeta.\tag{22}$$

21

Similarly, inverting the correction factor would result in a scaling of the experimental to match the distribution of the theoretical wave profile. The correction factor must be applied on a case-by-case basis; meaning one applies the individual correction factor to their respective test case. Therefore, the case specific correction can only be implemented post-process and the correction factor is dependent on the parameters describing the experimental test. The case specific correction is advantageous for experimental tests wherein the parameters do not vary; however, the correction is less applicable for testing a range of parameters. Instead, a generalized correction factor was developed for the model as an extension of the case specific correction.

5.1.2. General Case Correction

The second correction method, which is dependent on the value of kb, is referred to as the general case correction. To determine a generalized correction factor, a set of benchmark tests were referenced which included the results of wedge B, at a single mean depth of 12 cm. In doing so, validation could be examined for higher and lower wedge angles and mean depths. Analyzing the correction factors for the benchmark tests as a function of kb, a linear trend was observed creating a correction factor ζ_{kb} following the expression,

$$\zeta_{kb} = -0.1015kb + 0.8285. \tag{23}$$

The correction factor ζ_{kb} can be applied to the a/s model for any value of kb. As a result of the benchmark experimental tests used to develop the model correction in (23), the correction factor ζ_{kb} will be less than one for values of kb greater than -1.69. Based on the range of parameters explored in the experimental tests, $0.10 \leq kb \leq 3.25$; therefore, the correction factor will always work to decrease the value of a/s in the theoretical model. Since the majority of test cases are overestimated by the model, a decrease in the model a/s is desired; however, the underestimated tests will be negatively affected as a result. Overall, while the general case correction decreases the average percent error of the experimental tests, the correction factor ζ_{kb} is unique to the experimental equipment and any unaccounted for errors due to complex hydrodynamic phenomena in the water channel. Hence, the method may be limited in its applicability to other plunger systems as future users must determine their own correction factor ζ_{kb}. To avoid the dependency on kb, a third correction method was explored.

5.1.3. Operational Correction

The third method for correcting the PTF model is referred to as the operational correction. The operational correction applies a straight bias to the normalized model regardless of the design parameters. The model is normalized such that a given wave profile will have a zero mean and a standard deviation of one. As with the general case correction, the same set of benchmark tests were studied to determine the correction. To determine the exact bias which should be applied to the model, a range of percent decreases was applied to the model for the benchmark tests. The average a/s percent error between the experimental results and the modified model was then determined for each applied bias.

22

For no change in the model (0% bias), the average percent error in the experi-
mental results of the benchmark case is 40.55%; however, a local minimum was
found to exist by decreasing the amplitude of the normalized model by 26%.
In doing so, the average percent error decreases to 22.12%. Therefore, it would
be beneficial to decrease the normalized model for all cases and all wedges by
26%. After applying the decrease to the model, the data is denormalized and
compared to the measured a/s.

5.2. Discussion of Experimental Findings

Table 2 summarizes the results of the average a/s percent error between the
uncorrected PTF model and the experimental results as well as the results of
applying the three described corrections to the model. The averages in Table 2

Table 2: Summary of the average a/s percent error between the uncorrected and corrected
PTF models and the experimental results.

Wedge	Uncorrected PTF Model [%]	Corrected PTF Model [%]		
		Case Specific	General Case	Operational
A	58.13	3.33	33.73	38.86
B	48.04	2.85	26.52	30.44
C	72.78	2.47	36.41	45.69

include both the overestimated and underestimated test cases for each respective
wedge. Application of any of the three corrections to the theoretical plunger-
type wavemaker model is beneficial to lowering the a/s percent error between
the model and experimental results. For the case specific correction, the error
metric between the uncorrected and corrected PTF model decreases for wedge A
by $(58.13 - 3.33) = 54.80$. The difference corresponds to a percent improvement
given by,

$$\% \text{ improvement} = \frac{|58.13 - 3.33|}{58.13} \times 100\% = 94.27\%. \tag{24}$$

Similarly, for wedge B there is a decrease in the error metric of 45.19 correspond-
ing to a percent improvement of 94.07%, while for wedge C, the decrease in error
metric of 70.31 represents a percent improvement of 96.60%. For the general
case correction, there is a decrease in the error metric of 24.40, 21.52, and 36.37
corresponding to percent improvements in the averages of 41.97%, 44.80%, and
49.97% for wedge A, B, and C, respectively. Finally, for the operational cor-
rection, the error metric between the uncorrected and corrected PTF model
decreases by 19.27, 17.60, and 27.10, corresponding to a percent improvement
of 33.14%, 36.63%, and 37.23% for wedge A, B, and C, respectively.

Although the case specific correction yields the most improved results, the
exact correction factor applied to the model must be determined post-process.

23

Despite the difference in method, the operational correction to the model has a similar effect on the a/s percent error as the general case corrected model. However, applying a standard bias to the model rather than the correction factor ζ_{kb} is more applicable to plunger systems external to the experimental work performed herein. Therefore, the operational correction is a more appropriate method for correcting the theoretical PTF model such that the experimental a/s can be more accurately predicted.

A trend between the a/s percent error and the flow rate was observed in the results presented in Fig. 8-10. Table 3 presents the average values of the a/s percent error for the uncorrected and corrected PTF models, separated by the three wedges and five tested flow rates. The first row for each wedge

Table 3: Comparison of the average a/s percent error as a function of flow for the basic model and three model corrections.

Wedge	Flow [m/s]	Uncorrected PTF Model [%]	Corrected PTF Model [%]		
			Case Specific	General Case	Operational
A	0.000	34.79	1.88	22.86	28.08
	0.076	53.49	2.74	32.84	38.64
	0.152	49.37	2.51	22.81	27.09
	0.229	67.49	3.51	36.17	41.30
	0.305	85.52	6.01	53.98	59.21
B	0.000	22.18	1.80	18.22	17.76
	0.076	23.75	1.73	17.15	17.23
	0.152	46.62	3.10	20.04	24.80
	0.229	64.30	3.26	31.25	38.26
	0.305	83.33	4.36	45.91	54.17
C	0.000	23.09	1.53	16.83	12.64
	0.076	39.63	1.78	16.19	21.29
	0.152	67.41	2.13	26.02	38.03
	0.229	100.48	2.97	49.36	64.97
	0.305	133.30	3.96	73.66	91.49

corresponds to the no-flow cases, which also represents the Wu model, which does not incorporate flow. By introducing flow, the overall a/s percent errors for the PTF model tend to increase with increasing flow rate, with a maximum change in the average error metric of $(133.30 - 23.09) = 110.21$ for wedge C

24

from a flow of 0.305 m/s to no-flow. However, the average a/s percent error improves for each wedge and flow rate after application of a model correction.
₆₂₀ As such, regardless of the flow rate, based on the needs a correction factor should be applied to the PTF wavemaker model in order to accurately predict an experimental system.

The magnitude of the improvement provided by the model corrections are also an indicator for the operational range of the wavemaker system with respect
₆₂₅ to the flow rates. With the exception of the higher flow cases, the average a/s percent error when corrected tends towards the average a/s percent error as observed in the no-flow case or Wu model. At flow rates of 0.305 m/s, there is a large amount of error and operating at this rate will not be as predictable by the model; therefore, it is suggested that for the experimental system studied herein,
₆₃₀ flow rates should be limited to 0.229 m/s or less. To further improve the model, the operational range can also be limited by the other parameters studied within this paper. The results in Fig. 8-10 indicated that the a/s percent error is lower for smaller values of kb, regardless of the flow rate. Accordingly, operating the wavemaker system at lower frequencies is advantageous for reducing the error
₆₃₅ between the model and experimental outcome. Based on the analysis performed, it was determined that wavemaker should be operated at a maximum of 2.0 Hz. With respect to mean wedge depth and wavemaker stroke amplitude, it was determined that their impact was not significant compared to the frequency and flow rate. Nevertheless, for applications that require operating near the
₆₄₀ maximum limits of the frequency and flow parameters, larger mean depths and stroke amplitudes will be advantageous for generating the predicted waves due to the signal-to-noise ratio. Therefore, the range of operational values for both the mean depth and stroke amplitude remains limited only by the geometry of the wedge. Finally, with respect to the wedge angle, the results in Table 2
₆₄₅ show that wedge B generally had the lowest average a/s percent error for both the uncorrected and corrected PTF models. However, since the three wedges do not share the same submerged volume in this study, different wave profiles were produced for the same set of parameters (d_μ, U, ω, and s). Therefore, evaluating the impact of the wedge angle requires further investigation, which
₆₅₀ is currently being explored in an ongoing study. Note that these limits are unique to the water channel and the wavemaker system studied within this research and future users should perform a series of similar tests to determine their specific operating regime.

Taking into consideration the new operational range of the wavemaker sys-
₆₅₅ tem, the average a/s percent error between the experimental results and the uncorrected and corrected models can be re-evaluated. Table 4 presents the average a/s percent error for wedge A, B, and C for the uncorrected PTF model and the three corrected versions of the model. Evaluating the performance of the wavemaker system within the new operation limits imposed by the flow and
₆₆₀ frequency parameters, the case specific correction has the greatest impact on average a/s percent error, while the general case and operational corrections yield similar results for each wedge. Thus, even within the new operating limits, the operational correction is the most appropriate for application to the

Table 4: Effect of the applied operational range ($U \leq 0.229$ m/s and $f \leq 2.0$ Hz) on the average a/s percent error for the uncorrected and corrected PTF models.

Wedge	Uncorrected PTF Model [%]	Corrected PTF Model [%]		
		Case Specific	General Case	Operational
A	40.27	2.47	22.69	25.82
B	32.59	2.40	19.43	20.20
C	48.34	2.13	21.76	26.83

wavemaker model due to its advantageous implementation for plunger systems in general. By applying the new limits to the operating range, the error metrics of the operational correction in Table 2 decrease by 13.04, 10.24, and 18.86 for wedge A, B, and C, respectively. Therefore, application of the correction and operating limit is valid for improving the PTF model's ability to predict the output of the experimental system.

6. Conclusion

A new model for the plunger-type wavemaker which incorporates the effect of flow on the relationship between the wave amplitude and stroke amplitude has been proposed. It was shown that to include the impact of flow, the dispersion relations required modification. In addition to the flow U, the model requires five input parameters including the wave frequency, wedge angle, mean wedge depth, water depth, and the number of nodes for the kinematic boundary.

To investigate the influence of flow, as well as the remaining input parameters, on the PTF model, a variance-based global sensitivity analysis was presented. The sensitivity analysis provided results regarding the influence of all input parameters as well as their interactions with one another within the wavemaker model. It was determined that the wave frequency has the largest influence on the output variance of the wavemaker model. Therefore, hydrodynamic applications dependent on plunger-type wavemakers should take caution when executing and determining the wave frequency for the model in order to achieve a desired wave profile. On the other hand, it was established that the required number of nodes points is a non-influential parameter and can be set to a deterministic value. The VBGSA also determined that for a uniform flow, the first order and total effect sensitivity indices were estimated to be $1.29 \pm 0.32\%$ and $6.00 \pm 0.14\%$, respectively. While flow has a low impact on the wavemaker model, its influence cannot be neglected due to its interactions with the remaining influential parameters. Since a sensitivity analysis has not been previously applied to the either the PTF model or Wu model, the results of this paper allow for the theoretical design of the wavemaker to be taken into consideration for application to experimental plunger systems.

26

₆₉₅ To validate a physical plunger system and evaluate its performance relative to the wavemaker model, 900 experimental tests were performed taking into consideration the effects of flow rate, frequency, mean wedge depth, wedge angle, and stroke amplitude. Comparing a/s as predicted by the PTF model and measured by an ultrasonic sensor, the average percent error was determined ₇₀₀ to be 58.13%, 48.04%, and 72.78% for wedge A, B, and C, respectively. It was observed that as both frequency and flow rate increased, the a/s percent error also increased. Since the plunger model does not take into account of complex hydrodynamic phenomena such as turbulence, three different methods for correcting the model were explored however; it was determined that the ₇₀₅ third method, an operational correction which applied a 26% decrease to the normalized wavemaker model, was more widely applicable to plunger systems. By applying the correction, the average a/s percent error was improved by 33.14%, 36.63%, and 37.23% for wedges A, B, and C, respectively. That being said, by applying the case specific corrections to the PTF model, the average a/s ₇₁₀ percent error could be improved in a post-process analysis by 94.27%, 94.07%, and 96.60% for wedge A, B, and C, respectively. Taking the observed trends into consideration, it was concluded that in order for the generated waves to be more accurately predicted by the corrected model, the wavemaker studied herein should be operated at flow rates under 0.229 m/s and frequencies under ₇₁₅ 2.0 Hz. In doing so, the average a/s percent error with the operational correction applied further decreases the error metric by 13.04, 10.24, and 18.86 for wedge A, B, and C, respectively. With an operational range in place and the validation of the inclusion of flow in the model, the plunger-type wavemaker can be more efficiently used for future applications.

Acknowledgements

Appendix A.

The following appendix provides a thorough review of the Wu model, on which the PTF model is based. The plunger-type wavemaker problem can be defined by small amplitude wave theory where there exists a velocity potential ϕ that satisfies the continuity equation, $\nabla^2\phi = 0$, where the gradient ∇ leads to ₇₃₅ the Laplace equation. Solving for the linear wave profile becomes a boundary

27

value problem constrained by four boundary conditions and a far-field radiation condition (RC). The bottom boundary condition (BBC), located at $z = 0$ in Figure 3, is mathematically defined by [6],

$$\left(\frac{\partial \phi}{\partial z}\right)_{z=0} = 0. \tag{A.1}$$

Similarly, at $z = h$ there exists a combined free surface boundary condition (CFSBC) which is expressed by,

$$\left(\frac{\partial \phi}{\partial z} - \frac{\omega^2}{g}\phi\right)_{z=h} = 0, \tag{A.2}$$

where ω is the wave frequency and g is the acceleration due to gravity [6]. Assuming no leakage around the wedge, the kinematic boundary condition (KBC) along the wavemaker and the clearance section d'_μ is respectively defined by [6],

$$\left(\frac{\partial \phi}{\partial n}\right)_{d'_\mu \leq z \leq h} = s\omega \sin(\beta)\cos(\omega t), \tag{A.3a}$$

$$\left(\frac{\partial \phi}{\partial x}\right)_{0 \leq z < d'_\mu} = 0. \tag{A.3b}$$

When $\beta = 0$, the condition in (A.3a) is equal to that of (A.3b) and a single equation can be used to describe the KBC for $\beta \geq 0$ and $0 < z < h$. Combining (A.3a) and (A.3b), the modified KBC on the wavemaker at $x = (z - d'_\mu)\tan(\beta)$ is expressed as [6],

$$\frac{\partial \phi}{\partial x} - \frac{\partial \phi}{\partial z}\tan(\beta) = s\omega \tan(\beta)\cos(\omega t). \tag{A.4}$$

A form of the velocity potential $\phi(x,z)$ which satisfies the Laplace equation and the BBC, CFSBC, and RC is given by,

$$\phi(x,z) = A_0 \cosh(k_p z)e^{i_m k_p x} + \sum_{n=1}^{\infty} A_n \cos(k_n z)e^{-k_n x}, \tag{A.5}$$

where i_m is the imaginary number, A_0 and A_n are unknown coefficients of the velocity potential whose values are to be determined, and the wavenumbers k_p and k_n represent progressive and standing waves, respectively [6]. Equation (A.5) is constrained by the dispersion relationship of both wavenumbers k_p and k_n defined by [6],

$$\omega^2 = gk_p \tanh(k_p h), \tag{A.6}$$

$$\omega^2 = -gk_n \tanh(k_n h). \tag{A.7}$$

28

With the dispersion constraint, the velocity potential solution defined by (A.5) can be substituted into the modified KBC expressed in (A.4) to yield an expression from which A_0 and A_n can be determined [6],

$$\left[i_m A_0 k_p \cosh(k_p z) e^{i_m k_p (z - d'_\mu) \tan(\beta)} - \right.$$
$$\left. \sum_{n=1}^{\infty} A_n k_n \cos(k_n z) e^{-k_n (z - d'_\mu) \tan(\beta)} \right] -$$
$$\left[A_0 k_p \sinh(k_p z) e^{i_m k_p (z - d'_\mu) \tan(\beta)} - \right.$$
$$\left. \sum_{n=1}^{\infty} A_n k_n \sin(k_n z) e^{-k_n (z - d'_\mu) \tan(\beta)} \right] \tan(\beta)$$
$$= s\omega \tan(\beta). \tag{A.8}$$

To solve for the coefficients A_0 and A_n, a semi-analytical solution using the
760 boundary collocation method is applied [6]. For the wavemaker problem, the boundary is that which is defined by the KBC. The kinematic boundary is divided into segments of equal length with two node points at each end of a segment totalling M node points. To satisfy (A.8) at all M node points, the equation is expressed in matrix form as,

$$\mathbf{B}\mathbf{A}' = \mathbf{D}, \tag{A.9}$$

765 where $\mathbf{B}$ is a $m \times n$ matrix, $\mathbf{A}'$ is a $n \times 1$ matrix, and $\mathbf{D}$ is a $m \times 1$ matrix with the number of node points M equal to the number of matrix rows m and total number of waves n representing the number of matrix columns [6]. The elements of matrices $\mathbf{B}$, $\mathbf{A}'$, and $\mathbf{D}$ are expressed as,

$$B_{m1} = k_p h \left(i_m \cosh \left[k_p h \left(\frac{z}{h} \right)_m \right] - \right.$$
$$\left. \tan(\beta) \sinh \left[k_p h \left(\frac{z}{h} \right)_m \right] \right) e^{i_m k_p h \tan(\beta) \left(\frac{z - d'_\mu}{h} \right)_m}, \quad \text{(A.10)}$$

$$B_{mn} = -k_{n-1} h \left(\cos \left[k_{n-1} h \left(\frac{z}{h} \right)_m \right] - \right.$$
$$\left. \tan(\beta) \sin \left[k_{n-1} h \left(\frac{z}{h} \right)_m \right] \right) e^{-k_{n-1} h \tan(\beta) \left(\frac{z - d'_\mu}{h} \right)_m}, n \neq 1, \quad \text{(A.11)}$$

29

$$A'_1 = \frac{A_0}{s\omega h}, \tag{A.12}$$

$$A'_n = \frac{A_{n-1}}{s\omega h}, \quad n \neq 1, \tag{A.13}$$

$$D_m = \tan(\beta), \tag{A.14}$$

where B_{m1} represents a single progressive wave and B_{mn} represents the standing waves [6]. Equation (A.9) is solved using a least squares method to minimize the sum of quadratic error by multiplying both sides by the Hermitian transpose of $\mathbf{B}$ denoted $\mathbf{B}^T$ such that,

$$\mathbf{B}^T\mathbf{B}\mathbf{A}' = \mathbf{B}^T\mathbf{D}. \tag{A.15}$$

Wu [6] suggests using a finite number of waves by setting $n = 16$ such that the approximate solution to (A.15) includes one progressive wave and 15 standing waves. The RC ensures that the standing waves will decay with distance from the wavemaker such that terms in (A.5) relating to k_n will be negligible. For the RC to hold true in the experimental setup, McPhee [20] determined that standing waves will be considered negligible compared to progressive waves for distances double the water height h. Thus, taking the real part of the first term in (A.5), the velocity potential ϕ reduces to [6],

$$\phi = \text{Re}\big[A_0 \cosh(k_p z)e^{i_m(k_p x - \omega t)}\big]. \tag{A.16}$$

The linear wave profile of the free surface $\eta(x,t)$ where only the progressive wave exists is expressed as [6],

$$\eta(x,t) = \frac{1}{g}\frac{\partial \phi}{\partial t} = \text{Re}\Big[\frac{-i_m\omega A_0}{g}\cosh(k_p h)e^{i_m(k_p x - \omega t)}\Big], \tag{A.17}$$

where the amplitude of the wave a is defined by [6],

$$a = \left|\frac{-i_m\omega A_0}{g}\cosh(k_p h)\right|. \tag{A.18}$$

By dividing both sides of (A.18) by the stroke amplitude s, the theoretical plunger-type wavemaker model which relates the water wave amplitude a to the stroke amplitude s is derived to be [6],

$$\frac{a}{s} = \left|-i_m A'_1 k_p h \sinh(k_p h)\right|, \tag{A.19}$$

where A'_1 is defined by (A.12).

Appendix B.

For the Monte Carlo analysis in the VBGSA, $\mathbf{G}$ and $\mathbf{H}$ are two independent matrices whose elements are comprised of g_{ji} and h_{ji}, where $j = 1, 2, \ldots, N_s$,

$$
\mathbf{G} = \begin{bmatrix} x_1^{(1)} & x_1^{(2)} & \cdots & x_1^{(p)} \\ x_2^{(1)} & x_2^{(2)} & \cdots & x_2^{(p)} \\ \vdots & \vdots & \ddots & \vdots \\ x_{N_s}^{(1)} & x_{N_s}^{(2)} & \cdots & x_{N_s}^{(p)} \end{bmatrix} \qquad \mathbf{H} = \begin{bmatrix} x_{N_s+1}^{(1)} & x_{N_s+1}^{(2)} & \cdots & x_{N_s+1}^{(p)} \\ x_{N_s+2}^{(1)} & x_{N_s+2}^{(2)} & \cdots & x_{N_s+2}^{(p)} \\ \vdots & \vdots & \ddots & \vdots \\ x_{2N_s}^{(1)} & x_{2N_s}^{(2)} & \cdots & x_{2N_s}^{(p)} \end{bmatrix}.
$$
(B.1)

Without requiring further sampling, a third matrix is constructed denoted $\mathbf{G_H}$ which is equal to $\mathbf{G}$ but with the ith column replaced by the ith column from $\mathbf{H}$ such that,

$$
\mathbf{G_H} = \begin{bmatrix} x_1^{(1)} & \cdots & x_{(N_s+1)}^{(i)} & \cdots & x_1^{(p)} \\ x_2^{(1)} & \cdots & x_{(N_s+2)}^{(i)} & \cdots & x_2^{(p)} \\ \vdots & \ddots & \vdots & \ddots & \vdots \\ x_{N_s}^{(1)} & \cdots & x_{N_s}^{(i)} & \cdots & x_{N_s}^{(p)} \end{bmatrix}.
$$
(B.2)

The modified 95% confidence intervals for the first order δV_i and total effect δV_{Ti} variances are given by,

$$
\delta V_i = \frac{1.96}{\sqrt{N_s}} \left(\frac{1}{N_s} \sum_{j=1}^{N_s} \left[f(\mathbf{H})_j \left(f(\mathbf{G_H}^{(i)})_j - f(\mathbf{G})_j \right) \right]^2 - \right.
$$
$$
\left. \left[\frac{1}{N_s} \sum_{j=1}^{N_s} f(\mathbf{H})_j \left(f(\mathbf{G_H}^{(i)})_j - f(\mathbf{G})_j \right) \right]^2 \right)^{1/2}, \quad \text{(B.3)}
$$

$$
\delta V_{Ti} = \frac{1.96}{\sqrt{N_s}} \left(\frac{1}{2N_s} \sum_{j=1}^{N_s} \left[\left(f(\mathbf{G})_j - f(\mathbf{G_H}^{(i)})_j \right)^2 \right]^2 - \right.
$$
$$
\left. \left[\frac{1}{2N_s} \sum_{j=1}^{N_s} \left(f(\mathbf{G})_j - f(\mathbf{G_H}^{(i)})_j \right)^2 \right]^2 \right)^{1/2}. \quad \text{(B.4)}
$$

Similarly, the confidence interval for the overall variance δV is expressed as,

$$
\delta V \quad = \quad \frac{1.96}{\sqrt{N_s}} \left(\frac{1}{N_s} \sum_{j=1}^{N_s} \left[\left(f(\mathbf{G})_j \right)^2 \right]^2 - \left[\frac{1}{N_s} \sum_{j=1}^{N_s} \left(f(\mathbf{G})_j \right)^2 \right]^2 \right)^{1/2}. \quad \text{(B.5)}
$$

31

References

[1] Rolling Hills Research Corporation, El Segundo, CA, USA, Research Water Tunnels Specifications (2014).

[2] C. Westin, R. Irani, Modelling dynamic cable-sheave contact and detachment during towing operations, Marine Structures 77 (2021) 102960. doi:https://doi.org/10.1016/j.marstruc.2021.102960.

[3] C. Calnan, R. Bauer, R. Irani, Reference-point algorithms for active motion compensation of towed bodies, IEEE J. Ocean. Eng. 44 (4) (2018) 1024–1040. doi:10.1109/JOE.2018.2866317.

[4] R. Irani, W. Spencer, Future launch and recovery system, in: American Society of Naval Engineers: Launch & Recovery of Manned and Unmanned Vehicles from Surface Platforms, Linthicum, Maryland, 2014.

[5] E. Chappell, Theory and design of a wave generator for a short flume, MASc, University of British Columbia, Vancouver, British Columbia (1969).

[6] Y.-C. Wu, Plunger-type wavemaker theory, J. Hydraul. Res. 26 (4) (1988) 483–491. doi:https://doi.org/10.1080/00221688809499206.

[7] D. Ellix, K. Arumugam, An experimental study of waves genereated by an oscillating wedge, J. Hydraul. Res. 22 (5) (1984) 299–313. doi:https://doi.org/10.1080/00221688409499367.

[8] Y.-C. Wu, Waves generated by a plunger-type wavemaker, J. Hydraul. Res. 29 (6) (1991) 851–860. doi:https://doi.org/10.1080/00221689109498963.

[9] T. Mikkola, Simulation of plunger-type wavemakers, J. Structural Mechanics 40 (4) (2007) 19–39.

[10] J. Gadelho, A. Lavrov, C. G. Soares, R. Urbina, M. Cameron, K. Thiagarajan, CFD modelling of the waves generated by a wedge-shaped wave maker, in: C. G. Soares, T. Santos (Eds.), Maritime Technology and Engineering, Taylor & Francis Group, 2015, pp. 993–1000.

[11] M. Kashiwagi, Full-nonlinear simulations of hydrodynamics forces on a heaving two-dimensional body, J. Society of Naval Architects of Japan 180 (1996) 373–381. doi:https://doi.org/10.2534/jjasnaoe1968.1996.180_373.

[12] Z. Azadian-Kharanjani, A. Nikseresht, H. Bingham, A numerical investigation of wedge angle effects on a plunger type wave maker with a constant submerged volume, in: ASME 2018 37th International Conference on Ocean, Offshore and Arctic Engineering, Madrid, Spain, 2018. doi:https://doi.org/10.1115/OMAE2018-77380.

[13] A. Nikseresht, H. Bingham, A numerical investigation of gap and shape effects on a 2d plunger-type wave maker, J. Marine Science and Application 19 (2020) 101–115. doi:https://doi.org/10.1007/s11804-020-00135-5.

[14] M. He, A. Khayyer, X. Gao, W. Xu, B. Liu, Theoretical method for generating solitary waves using plunger-type wavemakers and its smoothed particle hydrodynamics validation, Appl. Ocean Res. 106 (2021) 102414. doi:https://doi.org/10.1016/j.apor.2020.102414.

[15] J. Hicks, H. Bingham, R. Read, A. Engsig-Karup, Nonlinear wave generation using a heaving wedge, Appl. Ocean Res. 108 (2021) 102540. doi:https://doi.org/10.1016/j.apor.2021.102540.

[16] B. Sun, C. Li, S. Yang, H. Zhang, A simplified method and numerical simulation for wedge-shaped plunger wavemaker, Ocean Eng. 241 (2021) 110023. doi:https://doi.org/10.1016/j.oceaneng.2021.110023.

[17] I. Sobol', Sensitivity analysis for non-linear mathematical models, Math. Modelling and Comput. Experiments 1 (4) (1993) 407–414.

[18] S. Lowell, R. Irani, Sensitivity analysis of plunger-type wavemakers with water current, in: IEEE Global OCEANS 2020:Singapore - U.S. Gulf Coast, Virtual, 2020.

[19] R. Dean, R. Dalrymple, Water Wave Mechanics for Engineers and Scientists, Prentice-Hall, 1984.

[20] J. McPhee, Control, simulation, and testbed development for improving maritime launch and recovery operations, MASc, Carleton University, Ottawa, Ontario (2019).

[21] B. Robinson, Aeroelastic oscillations of a pitching cantilever with structural geometric nonlinearities: theory, numerical simulation and global sensitivity analysis, MASc, Carleton University, Ottawa, Ontario (2018).

[22] H. Wan, J. Xia, L. Zhang, D. She, Y. Xiao, L. Zou, Sensitivity and interactions analysis based on sobol' method and its application in a distributed flood forecasting model, Water 7 (6) (2015) 2924–2951. doi:https://doi.org/10.3390/w7062924.

[23] P. Jadun, L. Vimmerstedt, B. Bush, D. Inman, S. Peterson, Application of variance-based sensitivity analysis method to the biomass scenerio learning model, Syst. Dyn. Rev. 33 (3-4) (2017) 311–335. doi:https://doi.org/10.1002/sdr.1594.

[24] B. Iooss, F. V. Dorpe, N. Devictor, Response surfaces and sensitivity analyses for an environmental model of dose calculations, Reliab. Eng. Syst. Safe. 91 (10-11) (2006) 1241–1251. doi:https://doi.org/10.1016/j.ress.2005.11.021.

33

[25] P. Heiselberg, H. Brohus, A. Hesselholt, H. Rasmussen, E. Seinre, S. Thomas, Application of sensitivity analysis in deisgn of sustainable buildings, Renew. Energy 34 (9) (2009) 2030–2036. doi:https://doi.org/10.1016/j.renene.2009.02.016.

[26] H. Zhang, Z. Liu, C. Zhan, B. Feng, A sensitivity analysis of a hull's local characteristic parameters on ship resistance performance, J. Mar. Sci. Technol. 21 (2016) 592–600. doi:https://doi.org/10.1007/s00773-016-0378-x.

[27] Q. Liu, B. Feng, Z. Liu, H. Zhang, The improvement of a varience-based sensitivity analysis method and its application to a ship hull optimization model, J. Mar. Sci. Technol. 22 (2017) 694–709. doi:https://doi.org/10.1007/s00773-017-0439-9.

[28] X. Cheng, G. Li, R. Skulstad, S. Chen, H. Hildre, H. Zhang, A neural-network-based sensitivity analysis approach for data-driven modeling of ship motion, IEEE J. Ocean. Eng. 45 (2) (2020) 451–461. doi:10.1109/JOE.2018.2882276.

[29] X.-G. Wang, Z.-J. Zou, F. Xu, R.-Y. Ren, Sensitivity analysis and parametric identification for ship manoeuvering in 4 degrees of freedom, J. Mar. Sci. Technol. 19 (2014) 394–405. doi:https://doi.org/10.1007/s00773-014-0277-y.

[30] A. Saltelli, P. Annoni, I. Azzini, F. Campolongo, M. Ratto, S. Tarantola, Variance based sensitivity analysis of model output. design and estimator for the total sensitivity index, Comput. Phys. Commun. 26 (6) (2010) 723–730. doi:https://doi.org/10.1016/j.cpc.2009.09.018.

[31] T. Homma, A. Saltelli, Importance measures in global sensitivity analysis of model output, Reliab. Eng. Syst. Safe. 52 (1) (1996) 1–17. doi:https://doi.org/10.1016/0951-8320(96)00002-6.

[32] M. Jansen, Analysis of variance designs for model output, Comput. Phys. Commun. 117 (1-2) (1999) 35–43. doi:https://doi.org/10.1016/S0010-4655(98)00154-4.

[33] D. Griffiths, Introduction to Quantum Mechanics, Prentice Hall, 1995.

[34] Thomson, Radford, VA, USA, PC Series Precision Linear Actuators Installation Manual (2021).

[35] Kollmorgen, Radford, VA, USA, AKM Instructions Manual (2019).

[36] Kollmorgen, Radford, VA, USA, AKD Quick Start Manual (2019).

[37] SICK, UM18-2 Pro Ultrasonic sensors (2018).
URL https://cdn.sick.com/media/docs/7/97/797/operating_instructions_um18_2_pro_en_im0051797.pdf

34

915 [38] K. Suh, W. Park, B. Park, Separation of incident and reflected waves in wave-current flumes, Coastal Eng. 43 (3-4) (2001) 149–159. doi:https://doi.org/10.1016/S0378-3839(01)00011-4.